G. Di Martino, A. Iodice, D. Poreh, D. Riccio “Pol-SARAS: A Fully Polarimetric SAR Raw Signal Simulator for Extended Soil Surfaces”, *IEEE Trans. Geosci. Remote Sens.*, vol. 56, no. 4, pp. 2233-2247, April 2018. DOI: 10.1109/TGRS.2017.2777606.

# Pol-SARAS: A Fully Polarimetric SAR Raw Signal Simulator for Extended Soil Surfaces

Gerardo Di Martino, *Senior Member, IEEE*, Antonio Iodice, *Senior Member, IEEE*, Davod Poreh, *Member, IEEE*, and Daniele Riccio, *Fellow, IEEE*

***Abstract*— We present a new synthetic aperture radar (SAR) raw signal simulator, which is able to simultaneously generate raw signals of different polarimetric channels of a polarimetric SAR system in such a way that a correct covariance matrix is obtained for the final images. Extended natural scenes, dominated by surface scattering, are considered. A fast Fourier-domain approach is used for the generation of raw signals. Presentation of theory is supplemented by meaningful experimental results, including a comparison of simulations with real polarimetric scattering data.**

***Index Terms*— Rough surfaces, SAR polarimetry, SAR simulation, synthetic aperture radar (SAR).**

## I. Introduction

IN RECENT years, synthetic aperture radar (SAR) polarimetry has been successfully applied to soil-moisture retrieval, forest monitoring, change detection, and marine applications [1]. Therefore, a polarimetric SAR raw signal simulator, based on a sound physical electromagnetic scattering model, would be certainly useful for mission planning, algorithm development and testing, and prediction of suitability of the system to different applications. This simulator should be able to consider extended scenes, whose macroscopic topography is possibly prescribed by an external digital elevation model (DEM), and to account for terrain roughness and soil electromagnetic parameters. Simulated raw signals of different polarimetric channels, when focused via standard SAR processing algorithms, should lead to a realistic polarimetric covariance (or coherency) matrix.

An efficient simulator with many of the above-cited features, called synthetic aperture radar advanced simulators (SARAS) [2]–[5], is actually available in the literature: in fact, it is a model-based raw signal simulator that among other system characteristics, also accounts for the transmitting and receiving polarizations. However, it can only simulate one polarimetric channel at a time, with the result that data of different channels turn out to be independent. Accordingly, although the correct relations between polarimetric channels' powers are obtained, the covariance (or coherency) matrix of the final images is not realistic.

Manuscript received June 15, 2017; revised September 8, 2017; accepted November 18, 2017. *(Corresponding author: Gerardo Di Martino.)*

The authors are with the Dipartimento di Ingegneria Elettrica e delle Tecnologie dell'Informazione, Università di Napoli Federico II, 80125 Naples, Italy (e-mail: gerardo.dimartino@unina.it; iodice@unina.it; davod.poreh@unina.it; daniele.riccio@unina.it).

Color versions of one or more of the figures in this paper are available online at http://ieeexplore.ieee.org.

Digital Object Identifier 10.1109/TGRS.2017.2777606

Here, we present a new improved version of that simulator that is able to simultaneously produce the raw signals of the different polarimetric channels in such a way to obtain the correct covariance or coherence matrices on the final images. We call this new simulator "Pol-SARAS" to indicate that it is the polarimetric version of the available SARAS. In the following, we will refer to the simulator for the classical stripmap acquisition mode [2], but the same modifications also apply to simulators for spotlight [3] and hybrid [4] acquisition modes, as well as to the one accounting for platform trajectory deviations [5]. In addition, we here only consider surface scattering, but due to the modular structure of the simulator, also other scattering mechanisms (volumetric and double bounce) can be included, if reliable models are available.

It must be recalled that polarimetric SAR simulators including also other scattering mechanisms are available in the literature (see [6], [7]). However, the simulator described in [6] is tailored for specific man-made targets, such as ships and tanks, and it cannot be used to simulate extended natural scenes. On the other hand, the simulator described in [7] can consider a wide range of natural and man-made scenarios with different scattering mechanisms. However, with that method, computation of the raw signal is necessarily in time domain, and hence it is very computationally demanding. Conversely, our proposed simulator can handle extended scenes (although, for the moment being, just including surface scattering), and it uses a fast Fourier-domain approach to generate raw signals, so that it is very efficient. In addition, at variance with the available literature, we also validate our simulator by using a comparison with actual polarimetric scattering data. Apart from [6] and [7], to the best of our knowledge, the several SAR simulators available in the literature (see [31]–[36], just to mention some of the most recent ones) are either not efficient, in the sense that they use time-consuming numerical scattering computation and/or time-domain raw signal evaluation, or not polarimetric, in the sense that they are not able to simultaneously generate all the different polarimetric channels with a realistic polarimetric covariance matrix.

The remainder of this paper is organized as follows. In Section II, the rationale of the proposed simulator is presented, highlighting similarities and differences with the available SARAS. Section III is dedicated to the description of simulation results. In particular, in Section III-A, the polarimetric coherency matrices obtained from simulated data are compared with those obtained by available approximate analytical scattering models; in Section III-B, a comparison

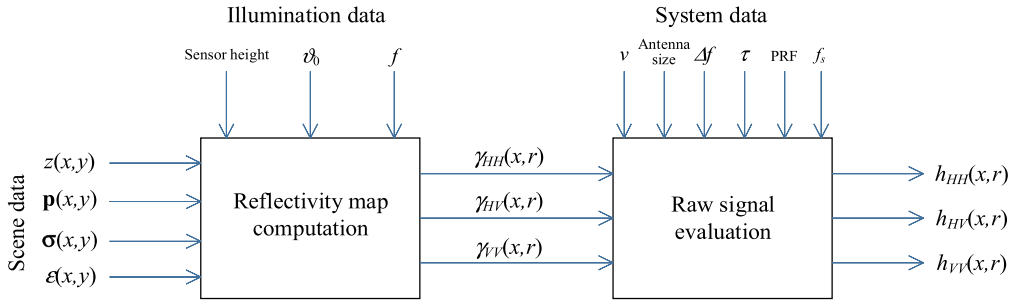


Fig. 1. General architecture of the simulator.

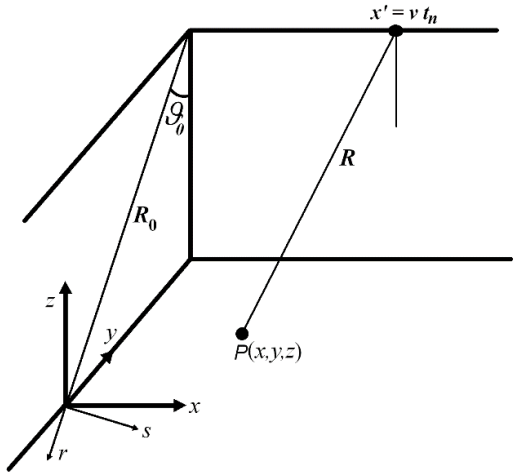


Fig. 2. Geometry of the problem and coordinate reference systems.

between simulated and real polarimetric data is presented; and in Section III-C, potential applications of the simulator to soil-moisture retrieval and azimuth terrain slope retrieval from SAR polarimetric data are illustrated. Finally, concluding remarks are reported in Section IV.

## II. Polarimetric Simulation Rationale

Similar to the SARAS simulator [2]–[5], the presented Pol-SARAS simulator employs a procedure consisting of two main stages. In the first stage, given the illumination geometry and the scene description, the scene reflectivity map, i.e., the ratio between backscattered and incident field components, is evaluated, thanks to appropriate direct models. At variance with SARAS, the three reflectivity maps corresponding to the HH, HV, and VV polarizations are here computed at the same time. In the second stage, the HH, HV, and VV SAR raw signals are computed via a superposition integral in which each reflectivity map is weighted by the SAR system 2-D impulse response, computed from system data. This general simulator architecture is schematized in Fig. 1, and the geometry of the problem is depicted in Fig. 2. It is assumed that the sensor moves at constant velocity $v$ along a straight-line nominal trajectory and it transmits chirp pulses at regularly spaced times $t_n$; note that in the employed reference system, $x$ is the azimuth coordinate, while $y$ and $r$ are the ground range and slant range coordinates, respectively.

The simulator input data can be grouped into three classes: scene data, illumination data, and system data. Scene data include the following.

1) The scene height profile $z(x, y)$, which can be either provided by an external DEM, possibly resampled to fit the employed reference system (see [24]), or selected by the user among a set of canonical ones (plane, pyramid, and cone).
2) Small-scale, $\mathbf{p}(x, y)$, and large-scale, $\sigma(x, y)$, roughness parameter maps, see below, which can be either provided by an external file or set by the user (in the latter case, the user can subdivide the scene in different rectangular patches, specifying the parameters of each of them).
3) Complex relative dielectric permittivity map $\varepsilon(x, y)$, which again can be either provided by an external file or set by the user (in the latter case, the user can subdivide the scene in different rectangular patches, specifying the permittivity of each of them).

Illumination data include sensor height, scene-center look angle $\vartheta_0$, and carrier frequency $f$.

Finally, system data include, for nonsquinted stripmap mode, sensor velocity $v$, antenna size, chirp bandwidth $\Delta f$ and duration $\tau$, pulse repetition frequency, and received pulse sampling frequency $f_s$. Additional parameters (e.g., squint angle and length of the trajectory flight portion used to acquire the raw data) are required for other acquisition modes [2]–[5].

### A. Computation of Reflectivity Maps

Let us now analyze the first simulation stage (i.e., reflectivity maps computation) in detail. Similar to the usual SARAS simulator, the surface macroscopic height profile is approximated by rectangular rough facets, large with respect to wavelength but smaller than SAR system resolution. The facet roughness is here referred to as small-scale roughness, and it is modeled as a stochastic process, whose statistics are prescribed by the set of input parameters $\mathbf{p}(x, y)$. Although different choices are possible, in this paper, we use a zero-mean band-limited 2-D fractional Brownian motion (fBm) isotropic stochastic process [11], characterized by its Hurst coefficient $H_t$ (with $0 < H_t < 1$) and its topothesy $T$, so that $\mathbf{p} \equiv (H_t, T)$. A notable property of the fBm process is that its power spectral density presents a power-law behavior and is given by

$$W(\kappa) = S_0 \kappa^{-2-2H_t} \tag{1}$$

where $\kappa = (\kappa_x^2 + \kappa_y^2)^{1/2}$ is the (isotropic) roughness wavenumber, and $S_0$ is related to $T$ and $H_t$ as reported in [11].

At variance with the existing SARAS, here, to model the large-scale roughness, we add zero-mean random deviations

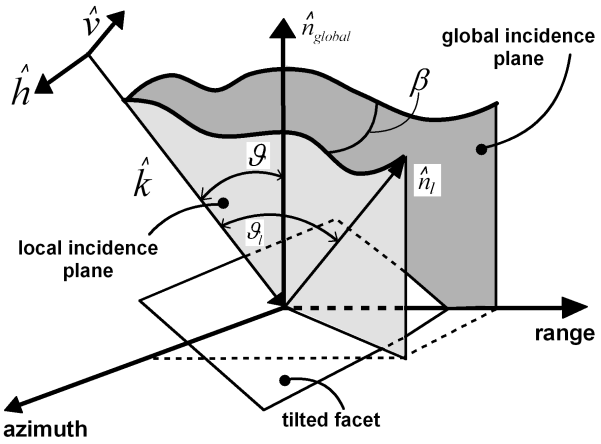


Fig. 3. Facet geometry.

to the facets' azimuth and range slopes prescribed by the macroscopic height profile. Therefore, we can express the azimuth and range slopes $a$ and $b$ of each facet as

$$a = a_0 + \delta a \tag{2a}$$

$$b = b_0 + \delta b \tag{2b}$$

where $a_0$ and $b_0$ are the azimuth and range slopes prescribed by the input macroscopic height profile $z(x, y)$, and the slope deviations $\delta a$ and $\delta b$ are zero-mean jointly Gaussian random variables with joint probability distribution function given by

$$p(\delta a, \delta b) = \frac{1}{2\pi \sigma_x \sigma_y \sqrt{1-\rho^2}} \times \exp\left[-\frac{1}{1-\rho^2}\left(\frac{\delta a^2}{2\sigma_x{}^2} + \frac{\delta b^2}{2\sigma_y{}^2} - \frac{\rho \delta a \delta b}{\sigma_x \sigma_y}\right)\right] \tag{3}$$

wherein $\boldsymbol{\sigma} \equiv (\sigma_x, \sigma_y, \rho)$ are the input large-scale roughness parameters, $\sigma_x$ and $\sigma_y$ being azimuth and range slope standard deviations, respectively, and $\rho$ is the correlation coefficient. A usual choice is $\sigma_x = \sigma_y = \sigma$, $\rho = 0$, so that the slope deviations $\delta a$ and $\delta b$ are independent identically distributed Gaussian random variables, and large-scale roughness is isotropic. However, with a different choice, it is also possible to explore the effects of large-scale roughness anisotropy. Realizations of random variables $\delta a$ and $\delta b$ according to (3) are generated by using a standard algorithm [25].

From input illumination data (in particular, $\vartheta_0$ and sensor height) and from $z(x, y)$, by using simple geometric relations, the facet center slant range $r$ and look angle $\vartheta$ (see Fig. 3) can be easily computed. Once facet slopes $a$ and $b$ and look angle $\vartheta$ are known, it is possible to compute the local incidence angle $\vartheta_l$, i.e., the angle formed by the look direction unit vector $\hat{k}$ and the local normal unit vector of the facet $\hat{n}_l$ (see Fig. 3); in addition, it is possible to evaluate the orientation angle $\beta$, i.e., the angle between global and local incidence planes (i.e., between the vertical plane including the look direction, and the plane perpendicular to the facet and including the look direction, see Fig. 3). In particular, with

$$\hat{k} = -\sin\vartheta\ \hat{l}_y - \cos\vartheta\ \hat{l}_z \tag{4}$$

and

$$\hat{n}_l = -\frac{a}{\sqrt{1+a^2+b^2}}\hat{l}_x - \frac{b}{\sqrt{1+a^2+b^2}}\hat{l}_y + \frac{1}{\sqrt{1+a^2+b^2}}\hat{l}_z \tag{5}$$

we can write

$$\vartheta_l = \cos^{-1}(\hat{k} \cdot \hat{n}_l) \tag{6}$$

$$\beta = \sin^{-1}(\hat{h} \cdot \hat{v}_l) \tag{7}$$

where

$$\begin{cases} \hat{h}_l = \dfrac{\hat{k} \times \hat{n}_l}{|\hat{k} \times \hat{n}_l|} \\ \hat{v}_l = \hat{h}_l \times \hat{k} \\ \hat{h} = \dfrac{\hat{k} \times \hat{n}}{|\hat{k} \times \hat{n}|} \\ \hat{v} = \hat{h} \times \hat{k}. \end{cases} \tag{8}$$

At this point, we have all the elements to evaluate the reflectivity $\gamma(x, r)$ of each facet, which can be computed by using the small perturbation method (SPM) or the physical optics (PO), according to the facet's small-scale roughness and incidence angle [8]: SPM holds for low roughness and intermediate incidence angles and PO for high roughness or small incidence angles. In particular, $\gamma(x, r)$ can be expressed as [8]–[10]

$$\gamma_{pq}(x, r; \vartheta_l, \beta, \varepsilon) = \chi_{pq}(x, r; \vartheta_l, \beta, \varepsilon) w(x, r; \vartheta_l) \tag{9}$$

where $p$ and $q$ are the polarizations of the incident and scattered fields, respectively, and stand for H (horizontal) or V (vertical), $\varepsilon$ is the input complex permittivity, $\chi_{pq}$ are the elements of the $2 \times 2$ matrix

$$\underline{\underline{\chi}}(\vartheta_l, \beta, \varepsilon) = \underline{\underline{R}}_2(\beta) \begin{pmatrix} F_H(\vartheta_l, \varepsilon) & 0 \\ 0 & F_V(\vartheta_l, \varepsilon) \end{pmatrix} \underline{\underline{R}}_2^{-1}(\beta) \tag{10}$$

with

$$\underline{\underline{R}}_2(\beta) = \begin{pmatrix} \cos\beta & \sin\beta \\ -\sin\beta & \cos\beta \end{pmatrix} \tag{11}$$

being the $2 \times 2$ unitary rotation matrix, and $F_H$ and $F_V$ either the Bragg (if SPM is used) or the Fresnel (if PO is used) coefficients for H and V polarizations, respectively [8]–[10]; $w(\vartheta_l)$ is a polarization-independent zero-mean circular complex Gaussian random variable, whose variance $\langle |w(\vartheta_l)|^2 \rangle$ depends on small-scale roughness. The expression of this dependence changes according to the employed scattering and small-scale (i.e., facet's) roughness models [8]–[11]: in the SPM case, it is proportional to the power spectral density $W(\cdot)$ of the facet's roughness, given by (1) for fBm roughness, and it can be expressed as

$$\langle |w(\vartheta_l)|^2 \rangle = k^4 \cos^4\vartheta_l W(2k\sin\vartheta_l) \tag{12}$$

where $k$ is the electromagnetic wavenumber. In the PO case, the expression of $\langle |w(\vartheta_l)|^2 \rangle$ is related to the Kirchhoff scattering integral and depends on the model considered for the observed surface [10], [11]. In this paper, with the exception mentioned at the end of this section, we will focus on SPM, but analogous results can be obtained by using PO. Realization of

the complex random variable $w(\vartheta_l)$ is obtained by generating two independent realizations of a zero-mean Gaussian random variable, used as real and imaginary parts of $w(\vartheta_l)$.

It is important to note that at variance with the already available SARAS simulator, in this updated version, the three polarimetric channels HH, VV, and HV = VH (HV and VH coincide, due to reciprocity) are simulated at the same time, and the same realization of the random variable $w(\vartheta_l)$ is used for all the three channels. This ensures that the polarimetric channels are not independent; on the other hand, the randomness of the facet slopes (which causes the randomness of $\vartheta_l$ and $\beta$, and is the other main novelty of Pol-SARAS) introduces a decorrelation among the different channels. By performing different simulations with a varying number of facets per pixel (from $1 \times 1$ to $20 \times 20$), we verified that practically the same correlations among polarimetric channels are obtained by using any number of facets per pixel equal to at least $2 \times 2$. In addition, in Sections III-A and III-B, we will show that the statistics of the simulated polarimetric channels are in agreement both with the ones predicted by theory and with the ones of real polarimetric data, so that we can conclude that if at least $2 \times 2$ facets per pixel are used, the correct joint statistics among polarimetric channels are obtained.

A few last remarks on the practical implementation of the above-described procedure are now due. First of all, since input data maps are sampled on a uniformly spaced grid over the *xy* plane, the output reflectivity maps turn out to be sampled on a grid which is uniformly spaced with respect to $x$, but nonuniformly spaced with respect to slant range $r$. To recover reflectivity maps sampled on a fully uniformly spaced grid also on the $x$, $r$ plane, to be used in the second simulation stage, the same efficient range interpolation procedure, based on a "power-sharing" approach, used in SARAS, is here implemented.

In addition, the same efficient ray-tracing recursive algorithm employed in SARAS [2] is here implemented to identify shadowed facets, whose reflectivity is set to 0. Note that for areas in back-slope close to shadow condition, the local incidence angle is very large, so that both SPM and PO are not appropriate. However, in this case, the backscattering is so low that even very large relative errors on the scattered field are of little practical importance, since in real data those areas are dominated by thermal noise.

Finally, particular care must be dedicated to areas near to layover conditions, for which local incidence angle is small. In fact, as already noted, SPM does not hold for small incidence angles, for which PO is more appropriate. In particular, (12) diverges as the incidence angle tends to 0; on the other hand, the PO value of $\langle |w(0)|^2 \rangle$ for fBm surfaces is available [11], and we call it $w_{\max}$. Indeed, small incidence angles are of no interest in the SAR case, except occasionally for areas near to layover conditions. To allow dealing also with such areas without complicating the simulation algorithm, in the proposed Pol-SARAS simulator, we use (12) if it leads to a value smaller than $w_{\max}$, otherwise we let $\langle |w(\vartheta_l)|^2 \rangle = w_{\max}$. This latter condition only occurs for incidence angles smaller than a threshold depending on small-scale roughness parameters $T$ and $H_t$. For values of roughness parameters usually exhibited by actual natural surfaces [11], the threshold angle ranges from very few degrees to about 20°.

The entire procedure described in this section is summarized in the block scheme of Fig. 4, where the parts that are new with respect to the SARAS simulator are evidenced by red dashed boxes.

### *B. Evaluation of Raw Signals*

Let us now consider the second simulation stage, in which the raw signals for the different polarization channels are obtained from the corresponding reflectivity maps by weighting them with the SAR system impulse response. Apart from the fact that this operation is performed three times (one for each polarimetric channel), this simulation stage is not changed with respect to the SARAS case. Therefore, we here just briefly recall the procedure employed for the stripmap acquisition mode [2]. However, a similar efficient 2-D Fourier-domain approach can also be used for the spotlight case [3] and/or in the case of sufficiently regular deviations with respect to the nominal trajectory [5]. In addition, a mixed time- and Fourier-domain approach can be used for the hybrid (i.e., sliding spotlight) acquisition mode and/or in the presence of general trajectory deviations [4].

A chirp modulation of the transmitted pulse is assumed. The expression of the SAR raw signal is the following [2]:

$$h_{pq}(x', r') = \iint \gamma_{pq}(x, r) g(x' - x,\ r' - r;\ r) dx dr \quad (13)$$

wherein

$$\begin{aligned} g(x' - x,\ r' - r;\ r) &= \exp\left[-j\frac{4\pi}{\lambda}\Delta R\right] \exp\left[-j\frac{4\pi}{\lambda}\frac{\Delta f/f}{c\tau}(r' - r - \Delta R)^2\right] \\ &\quad \times u^2\left(\frac{x' - x}{X}\right) \operatorname{rect}\left[\frac{(r' - r - \Delta R)}{c\tau/2}\right] \end{aligned} \quad (14)$$

is the SAR system impulse response, and

$$\Delta R = \Delta R(x' - x; r) = R - r = \sqrt{r^2 + (x' - x)^2} - r. \quad (15)$$

In (13)–(15) (see also Fig. 2), the variables used may be defined as follows.

1) $x'$ is the azimuth coordinate of the antenna position.
2) $R$ is the distance from the antenna to the generic point of the scene.
3) $R_0$ is the distance from the line of flight to the center of the scene.
4) $c$ is the speed of light.
5) $u(\cdot)$ is the azimuth illumination diagram of the real antenna over the ground.
6) $X = \lambda R_0 / L$ is the real antenna azimuth footprint [we assume that $u(\cdot)$ is negligible when the absolute value of its argument is larger than 1/2, and that it is an even function].
7) $\lambda$ is the electromagnetic wavelength, and $L$ is the azimuth dimension of the real antenna.
8) rect$[t/T]$ is the standard rectangular window function, i.e., rect$[t/T] = 1$ if $|t| \leq T/2$, otherwise rect$[t/T] = 0$.

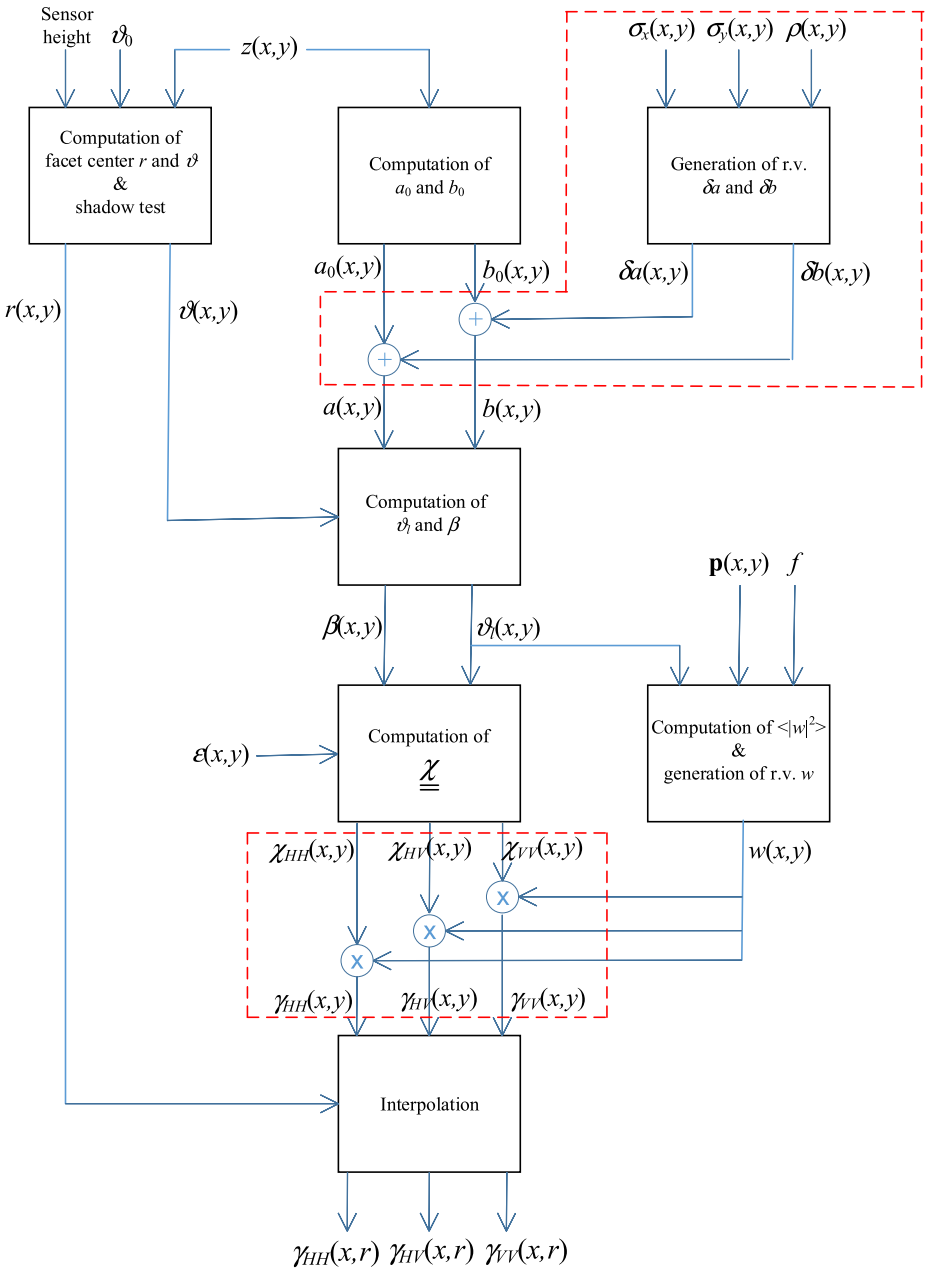


Fig. 4. Block scheme of the reflectivity map computation; "r.v." stands for "random variable." Novelties with respect to the SARAS simulator are evidenced by red dashed boxes.

9) $r'$ is $c/2$ times the time elapsed from each pulse transmission, and all other symbols have been already defined.

If we ignore the $r$-dependence of $g(\cdot)$, i.e., if we let $r = R_0$ in (15), then (13) is easily recognized as the 2-D convolution between $\gamma$ and $g$, which can be efficiently performed in the 2-D Fourier transform (FT) domain. Even considering the $r$-dependence, (13) can be efficiently computed in the 2-D FT domain: in fact, by using the stationary phase method, it can be shown [2] that the FT of (13) is

$$H_{pq}(\xi,\eta) = G_0(\xi,\eta)\Gamma_{pq}[\xi, \eta\Omega(\xi) + \mu(\xi)] \tag{16}$$

where $H_{pq}(\xi,\eta)$ is the FT of $h_{pq}(x,r)$ and $\Gamma_{pq}(\xi,\eta)$ is the FT of $\gamma_{pq}(x,r)$, and

$$G_0(\xi,\eta) = \exp\left[j\frac{\eta^2}{4b}\right]\exp\left[j\frac{\xi^2}{4a(1+\eta\lambda/(4\pi))}\right] \times \operatorname{rect}\left[\frac{\eta}{2bc\tau/2}\right] u^2\left(\frac{\xi}{2aX}\right) \tag{17}$$

is the FT of $g(x'-x,\ r'-r;\ r=R_0)$

$$a = \frac{2\pi}{\lambda R_0}, \quad b = \frac{4\pi}{\lambda}\frac{\Delta f/f}{c\tau} \tag{18}$$

and the functions

$$\mu(\xi) = \frac{\xi^2}{4aR_0}, \quad \Omega(\xi) = 1 - \frac{\xi^2}{4aR_0}\frac{\lambda}{4\pi} \tag{19}$$

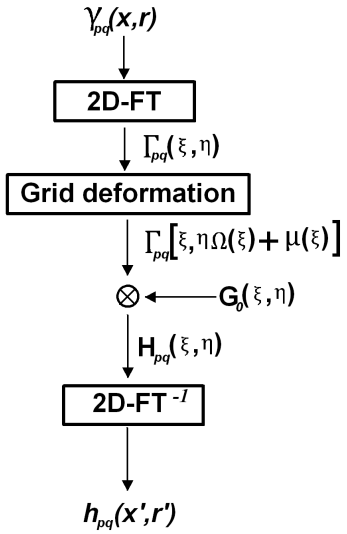


Fig. 5. Flowchart of SAR raw signal simulation, given a reflectivity map.

account for the $r$-space-variant characteristics of the SAR system, i.e., for the $r$-dependence of $g(\cdot)$.

Equation (16) suggests that the stripmap SAR raw signal simulation can be performed as shown in the flowchart in Fig. 5 [2], [4], where the "Grid deformation" block performs an interpolation in the Fourier domain, to obtain the desired values $\Gamma_{pq}[\xi, \eta\Omega(\xi) + \mu(\xi)]$ from the available ones $\Gamma_{pq}(\xi, \eta)$.

This is the method employed in the stripmap SAR raw signal simulator presented in [2], and also adopted here. Use of efficient Fast FT algorithms leads, in the case of extended scenes, to a processing time of different orders of magnitude smaller than the one required by a time-domain simulation directly based on (13)–(15).

Once the raw signals for the different polarization channels are simulated, they can be focused with usual processing algorithms employed for actual SAR data, in order to obtain the final single-look complex images.

## III. Simulation Results

In this section, we illustrate some results obtained by using the Pol-SARAS simulator described in Section II. The presented experiments are aimed at the following:

1) verifying the consistency of the proposed simulator by comparing the polarimetric coherency matrices obtained from simulated data with those obtained by available approximate analytical scattering models;
2) validating the proposed simulator by comparing simulated and actual polarimetric SAR data;
3) illustrating the potentiality of the proposed simulator in some SAR polarimetry applications, and in particular, in developing and verifying algorithms to retrieve soil-moisture or azimuth terrain slope from SAR polarimetric data.

### A. Comparison With Theoretical Models

As the first consistency check, let us verify that polarimetric data obtained from simulated raw signals are in agreement with those obtained by available approximate analytical scattering models.

The most popular approximate analytical scattering models are PO and SPM. However, they are not able to take into account cross-polarization and depolarization effects, which are essential for the modeling of polarimetric scattering from rough surfaces (i.e., according to PO and SPM, the HV backscattering is zero and HH and VV channels are perfectly correlated, both results being in disagreement with experiments) [9]. To properly deal with these effects, the second-order SPM and integral equation methods have been proposed, but their formulations are not in closed form, and they are too involved to be used efficiently in practice [9], [10]. Two-scale models have been introduced, which, even if able to extend the SPM validity significantly, still do not take into account the depolarization effect [10]. In [13], the model called "X-Bragg" has been presented to take care of the cross-polarization and depolarization effects. However, X-Bragg uses an unrealistic uniform distribution to model the $\beta$ angle (see Fig. 3), and completely ignores the random variation of the local incidence angle due to (large-scale) roughness. The polarimetric two-scale model (PTSM) solves the aforementioned problems [9], taking into account both cross-polarization and depolarization effects properly: as demonstrated by meaningful experiments, in low-vegetated areas, it presents a better agreement with measured data [9]. In the PTSM model, the SPM expressions of the covariance matrix elements of tilted rough facets are evaluated; in particular, they are expressed in terms of the facets' slopes $a$ and $b$ (along azimuth and range directions, respectively) by using the well-known relations linking them to $\beta$ and $\vartheta_l$ [9]. Finally, the entries of the covariance matrix of the overall surface are obtained by averaging the corresponding tilted facets expressions over $a$ and $b$, after a second-order expansion around $a = 0$ and $b = 0$. Therefore, some similarity between the PTSM and the Pol-SARAS approach may be noted. However, relevant differences are also present between the two approaches. In particular, in PTSM, a second-order expansion around $a = 0$ and $b = 0$ is performed, in order to analytically evaluate the covariance matrix elements. Conversely, in Pol-SARAS, this approximation is not needed, because the covariance matrix elements can be directly estimated on the polarimetric SAR images obtained by focusing simulated raw signals. In addition, at variance with PTSM, Pol-SARAS can account for anisotropic behaviors of the imaged surfaces [see (3)], as we will show in detail in Section III-C. Summarizing, in general, the Pol-SARAS approach is expected to present a wider validity range than that of theoretical approximated models, and a meaningful comparison can be performed only with X-Bragg and PTSM models, which account for cross-polarization and depolarization.

X-Bragg and PTSM models allow for the computation of covariance or coherency matrices [1] that have six independent elements, of which three are real and three are complex. Accordingly, comparison of coherency matrices obtained by Pol-SARAS, X-Bragg and PTSM would amount to compare three sets of nine real numbers each, and this should be repeated for several combinations of input parameters ($\varepsilon$, small-scale and large-scale roughness parameters, $\vartheta$, $f$). A simpler comparison can be obtained by considering proper

TABLE I
SIMULATION PARAMETERS FOR FLAT AND VESUVIUS SCENES

| | | |
|---|---|---|
| Sensor height | [km] | 200 |
| Sensor velocity | [km/s] | 0.9 |
| Azimuth antenna size | [m] | 1.5 |
| Range antenna size | [m] | 8.5 |
| Carrier frequency | [GHz] | 1.28 |
| Pulse duration | [μs] | 1.9 |
| Sampling rate | [MHz] | 14 |
| PRF | [Hz] | 350 |
| Doppler centroid | [Hz] | 0 |
| Chirp bandwidth | [MHz] | 14 |
| Topothesy | [m] | 0.001 |
| Hurst coefficient | | 0.8 |

combinations of the coherency matrix elements. A convenient choice is to use entropy and alpha angle [1]: entropy $H$ is related to the eigenvalues of the coherency matrix and mainly measures the "degree of randomness" of the scattering process, whereas the angle $\alpha$ is related to eigenvalues and eigenvectors of coherency matrix, and it also depends on the kind of scattering mechanism, i.e., single, double, or volumetric scattering. In the presence of surface scattering only, $H$ and $\alpha$ mainly depend on $\vartheta$, $\varepsilon$, and large-scale roughness $\sigma$ only. More details about $H$ and $\alpha$ can be found in [1], [13], [18], and [19]. In [9], PTSM and X-Bragg were compared with respect to $H$–$\alpha$ charts, i.e., graphs in which, for a fixed incidence angle, $H$ and $\alpha$ values obtained in correspondence of $\varepsilon$ and $\sigma$ pairs are plotted (see Fig. 6). Here, we use the same graphs to compare Pol-SARAS with both PTSM and X-Bragg. To evaluate $H$ and $\alpha$, we simulated the polarimetric channels' raw signals giving as an input to the simulator a flat DEM (i.e., no macroscopic topography) and using the parameters of Table I, with $3 \times 7$ facets per pixel in azimuth and range, respectively. Once the three channels' complex images were obtained via standard focusing of the raw data, we evaluated $H$ and $\alpha$ from coherency matrix elements obtained by averaging over $8 \times 8$ pixel windows; we then applied a further average of the obtained $H$ and $\alpha$ values over the whole scene. Finally, we repeated the simulations for several values of $\varepsilon$ and $\sigma$, in order to obtain the desired graphs.

In Fig. 6, a comparison between PTSM and X-Bragg $H$–$\alpha$ graph predictions and Pol-SARAS-based ones is provided for three different values of the look angle. PTSM and X-Bragg graphs are evaluated assuming the same surface parameters used for the simulations. For large look angles, i.e., 55° and 45°, PTSM predictions are in good agreement with Pol-SARAS results, even if, for increasing values of $\sigma$, entropy tends to be slightly underestimated and $\alpha$ slightly overestimated by PTSM. Conversely, as expected, Pol-SARAS results significantly depart from X-Bragg predictions, which tend to underestimate $H$ and overestimate $\alpha$. For smaller values of the look angle [e.g., 35°, see Fig. 6(c)], also the PTSM graph departs from the Pol-SARAS one, for $\sigma$ larger than about 0.1.

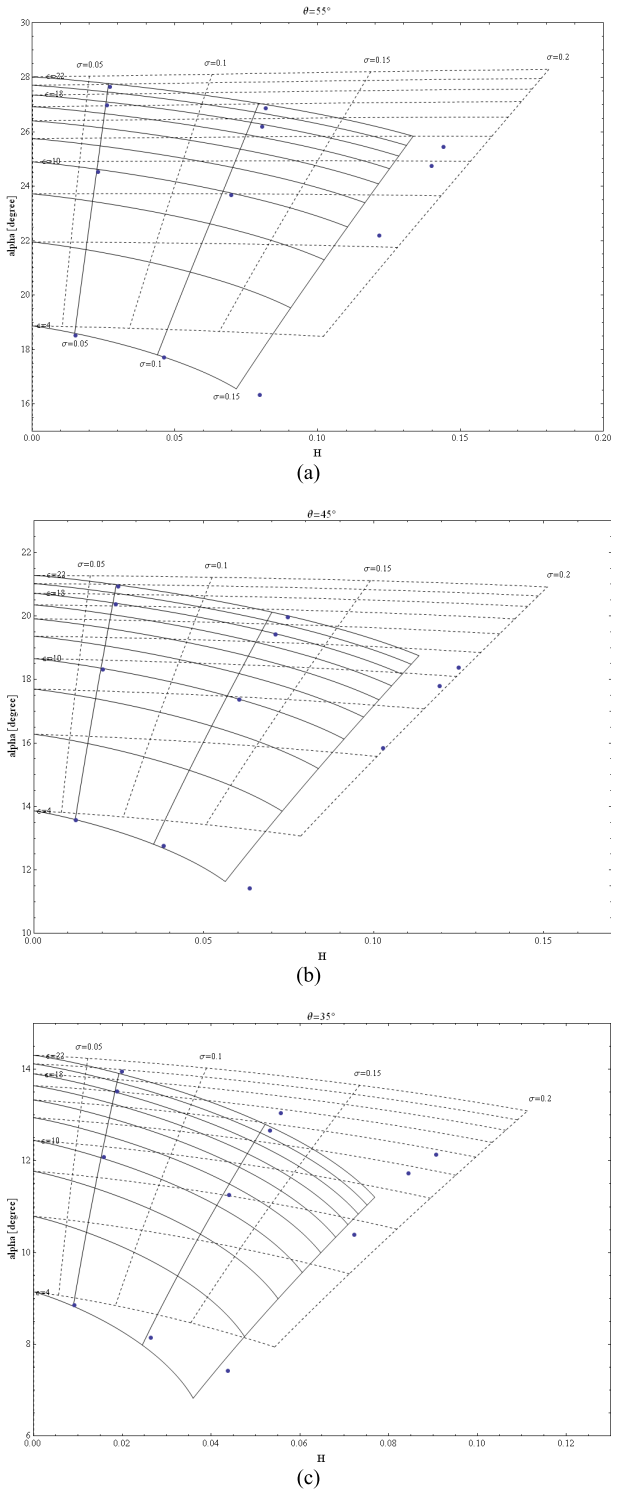


Fig. 6. $H$–$\alpha$ chart obtained via PTSM (solid line) and X-Bragg (dashed line), compared with Pol-SARAS results (blue points) for (a) $\vartheta = 55°$, (b) $\vartheta = 45°$, and (c) $\vartheta = 35°$. Pol-SARAS points are evaluated for $\varepsilon$ equal to 4, 10, 18, and 22, and for $\sigma$ equal to 0.05, 0.1, 0.15, and 0.2.

In particular, $\alpha$ and $H$ tend to be underestimated by PTSM. Indeed, in this case, the PTSM is close to the limit of its validity range, especially for increasing values of $H$.

By summarizing, we can state that the Pol-SARAS results are in reasonable agreement with the ones of the PTSM method, at least within the range of validity of the latter.

### B. Comparison With Measured Data

Comparison of polarimetric data obtained from simulated and real data is now in order. To perform a meaningful comparison, real SAR polarimetric data should be available for a scene for which a DEM is available, as well as the maps of permittivity and small- and large-scale soil roughness (i.e., all the simulator input scene data). Unfortunately, while DEMs are available for most part of the world, permittivity and roughness maps are seldom, if not never, available. That is why quantitative comparisons between simulated and real SAR data are very seldom reported in the literature. Here, we circumvent this problem in two ways: in one approach, we make reference to polarimetric scatterometer real data relative to a small bare-soil flat area for which *in situ* measurements of surface permittivity and roughness are available; alternatively, in order to consider real SAR polarimetric data, we use for comparison purposes a combination of polarimetric channels that in case of bare soils, only depends on topography, and is independent of surface permittivity and roughness (namely, the combination synthesizing the argument of correlation among right-handed and left-handed circular polarizations [20]), so that the correct knowledge of these input data is not critical.

With regard to the first approach, we compare simulation results with data acquired by the University of Michigan's LCX POLARSCAT [9], [22], which provides measured values of the polarimetric normalized radar cross section (NRCS) for HH, VV, and HV channels. At the same time of scatterometer acquisitions, also *in situ* measurements of soil parameters were performed [22]. This allows for comparing the measured values of the NRCSs with those obtained providing these parameters as input to Pol-SARAS. In particular, here, we consider the case of L-band data and moderate soil roughness, i.e., POLARSCAT data relevant to the slightly rough bare-soil surfaces 1 of [22]. For this surface, unfortunately, large-scale roughness was not measured, and only the standard deviation over 1-m long profiles $s$ is available: in particular, for the considered surface, we have $ks = 0.16$. Hence, for simulation purposes, we fixed $\varepsilon$ to the value measured in the top 4-cm soil layer: in particular, surface 1 was monitored in the presence of two different moisture conditions, corresponding to two different values of $\varepsilon$. With regard to the large-scale roughness, we fixed its value to 0.17, i.e., the average value obtained via PTSM-based retrieval for different incidence angles and for the two moisture conditions: PTSM-retrieved large-scale roughness for surface 1 may be found in [9].

In Tables II and III, we present the results obtained for wet and dry soil-moisture states, respectively. In particular, we report the values (in dB) of co-polarized (copol) and cross-polarized (crosspol) ratios measured by the scatterometer, along with those predicted by the simulations. The latter are defined as follows:

$$\begin{cases} \text{copol} = \dfrac{\langle |i_{\text{HH}}|^2 \rangle}{\langle |i_{\text{VV}}|^2 \rangle} \\ \text{crosspol} = \dfrac{\langle |i_{\text{HV}}|^2 \rangle}{\langle |i_{\text{VV}}|^2 \rangle} \end{cases} \tag{20}$$

where $i_{pq}$ is the focused complex image relevant to the $pq$ polarimetric channel. The parameters of Table I were used for simulations, apart from the carrier frequency that was set to 1.5 GHz, to match it with the scatterometer one. For $\varepsilon$ and $\sigma$, the values used in the simulations are reported in the first row of Tables II and III. We note that the absolute difference between scatterometer and Pol-SARAS copol ratio values is at most 1 dB, i.e., comparable with POLARSCAT measurement precision of $\pm 0.4$ dB [22]. With regard to the crosspol ratio, for the wet case, the maximum absolute difference is 1.1 dB, whereas for the dry case, for an incidence angle of 30° the absolute difference is 3.4 dB and for 40° it is 2.3 dB. However, for larger incidence angles (50° and 60°), the absolute difference is less than 1 dB. These results confirm the validity of the proposed simulator, which is able to provide results in reasonable agreement with real data for a wide range of incidence angles and soil surface parameters.

TABLE II
COMPARISON WITH MEASURED DATA, SURFACE 1-WET

| surface 1-wet L-band (1.5 GHz) | | | $\varepsilon$=15.57; $\sigma$=0.17 | |
|---|---|---|---|---|
| $\theta$ degrees | crosspol (ground) | copol (ground) | crosspol (Pol-SARAS) | copol (Pol-SARAS) |
| 30° | −21 | −2 | −21.2 | −2.3 |
| 40° | −19 | −4 | −20.1 | −3.6 |
| 50° | −20 | −6 | −19.0 | −5.6 |
| 60° | −19 | −9 | −18.1 | −8.2 |

TABLE III
COMPARISON WITH MEASURED DATA, SURFACE 1-DRY

| surface 1-dry L-band (1.5 GHz) | | | $\varepsilon$=7.99; $\sigma$=0.17 | |
|---|---|---|---|---|
| $\theta$ degrees | crosspol (ground) | copol (ground) | crosspol (Pol-SARAS) | copol (Pol-SARAS) |
| 30° | −19 | −1 | −22.4 | −2.0 |
| 40° | −19 | −3 | −21.3 | −3.1 |
| 50° | −20 | −4 | −19.9 | −4.8 |
| 60° | −18 | −6 | −19.0 | −6.9 |

Let us now move to the second approach, in order to directly compare simulated and real SAR polarimetric images of an area with significant topography. We here use May 1998 NASA/JPL AIRSAR L-band polarimetric data of Camp Roberts, CA, USA, for which a DEM is also available [26]. Main AIRSAR system and acquisition data are listed in Table IV, and they have been used also as inputs of our simulator, together with the scene parameters also listed in Table IV. Since, as usual, permittivity and roughness maps of the imaged area are not available, for comparison purposes, we use a combination of polarimetric channels that at least for bare soils, is only dependent on topography, and, in particular, mainly on the mean azimuth terrain slope within each SAR

TABLE IV
SIMULATION PARAMETERS FOR CAMP ROBERTS AIRSAR DATA

| | | |
|---|---|---|
| Sensor height | [km] | 7.6813 |
| Sensor velocity | [km/s] | 0.4323 |
| Look angle | [degree] | 44.8 |
| Azimuth antenna size | [m] | 3 |
| Range antenna size | [m] | 0.8 |
| Carrier frequency | [GHz] | 1.2 |
| Pulse duration | [μs] | 10 |
| Sampling rate | [MHz] | 45 |
| PRF | [Hz] | 840.3 |
| Doppler centroid | [Hz] | 0 |
| Chirp bandwidth | [MHz] | 14 |
| Topothesy | [m] | 0.001 |
| Hurst coefficient | | 0.8 |
| Permittivity ($\varepsilon$) | | 22 |

resolution cell. This combination is [20], [27]

$$I_2 = \arctan\left(\frac{4\mathrm{Re}\left\{\left\langle (i_{\mathrm{HH}} - i_{\mathrm{VV}}) i_{\mathrm{HV}}^{*}\right\rangle\right\}}{4\langle |i_{\mathrm{HV}}|^2\rangle - \langle |i_{\mathrm{HH}} - i_{\mathrm{VV}}|^2\rangle}\right). \tag{21}$$

We used $2 \times 2$ facets per pixel in our simulations, and we computed averages in (21) by using $2 \times 36$ (range $\times$ azimuth) pixel windows on SAR images obtained from both real and simulated raw signals, so obtaining a final pixel spacing of about 20 m $\times$ 20 m. $I_2$ images obtained from real and simulated raw signals are shown in Fig. 7(a) and (b), respectively, and in Fig. 7(c), the RGB false-color Pauli decomposition [1] of the real data is displayed. In the latter, $(2\langle |i_{\mathrm{HV}}|^2\rangle)^{1/2}$ is loaded on the green band, $(\langle |i_{\mathrm{HH}} + i_{\mathrm{VV}}|^2\rangle/2)^{1/2}$ is loaded on the red band, and $(\langle |i_{\mathrm{HH}} - i_{\mathrm{VV}}|^2\rangle/2)^{1/2}$ is loaded on the blue band, and all three bands are normalized with respect to $(\langle |i_{\mathrm{HH}}|^2\rangle + \langle |i_{\mathrm{VV}}|^2\rangle + 2\langle |i_{\mathrm{HV}}|^2\rangle)^{1/2}$: with this representation, the red band is mainly associated with the surface scattering contribution, the green band with the volume scattering contribution, and the blue band with double bounce [1]. Visually, there is a reasonable agreement between real and simulated $I_2$ images, but the former is clearly noisier than the latter. This is due to two factors: first of all, $I_2$ is quite sensitive to thermal noise (due to the presence of the crosspol power at the denominator of (21) and to the correlation at the numerator of (21) [20], [27]), which we have not included in the simulation, since the thermal noise level is not known; second, some parts of the imaged scene are covered with rather dense vegetation, as indicated by the green/blue areas of the Pauli-decomposition image (volumetric scattering due to tree foliage and branches, and double scattering due to trunk-ground reflections), and in such areas, $I_2$ is dependent not only on topography, but also on the spatially varying vegetation properties, which again are not included in the simulation (and anyway are not known). In order to perform a quantitative

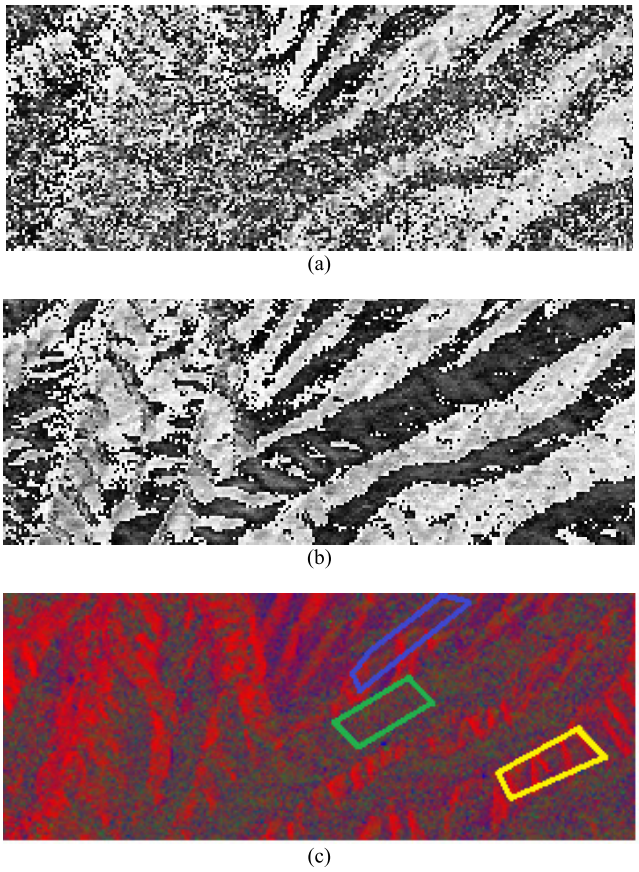

Fig. 7. $I_2$ images obtained from (a) real and (b) simulated polarimetric SAR data ($\sigma = 0.15$), and (c) Pauli RGB decomposition. Yellow, green, and blue boxes encircle the three ROI of Tables V and VI.

comparison, we considered three regions in the scene: a favorable one [indicated by a yellow polygon in Fig. 7(c)], in which surface scattering is the dominant mechanism; an intermediate one [indicated by a blue polygon in Fig. 7(c)], in which surface scattering is mixed with the other mechanisms; and an unfavorable one [indicated by a green polygon in Fig. 7(c)], in which volume and double scattering dominate. Mean values and standard deviations of real and simulated $I_2$ are reported in Table V for each of the three regions and for three values of the large-scale roughness parameter $\sigma$ employed as simulator inputs. A reasonable agreement between real and simulated data is obtained for the mean values of $I_2$ in both the favorable ("yellow") and the intermediate ("blue") regions, whereas, as expected, a poor agreement is obtained in the unfavorable ("green") area. It can be also noted that for the simulated data, in all regions, $I_2$ mean valuese decrease (in modulus) as $\sigma$ increases. Finally, confirming the result of the qualitative visual inspection, standard deviations on simulated data are smaller than those on real data, and this difference is more evident in the "green" area. This is in agreement with the explanation that we have given above for the noisier look of $I_2$ real image. In conclusion, we can state that $I_2$ images obtained from real and simulated data are in good agreement in the areas where surfac scattering is significant. This is further confirmed by the comparison of histograms of real and

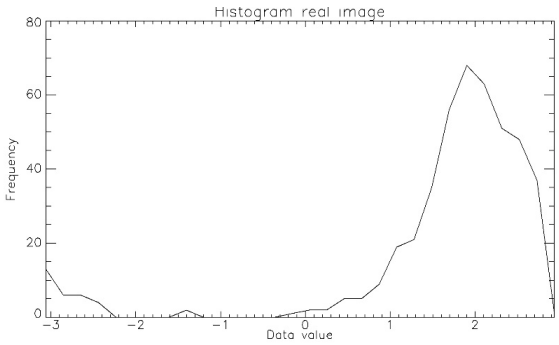


Fig. 8. Histogram of $I_2$ values in the "yellow" region of Fig. 7, obtained from (a) real and (b) simulated data.

simulated $I_2$ images, shown in Fig. 8(a) and (b), respectively, for the "yellow" region.

### C. Usefulness of the Simulator in Some Applications

In this section, we present some simulation results illustrating the potentiality of the proposed simulator in some applications of SAR polarimetry. Let us first consider soil-moisture retrieval, which is one of the main applications of fully polarimetric SAR data [1], [8], [9], [12]–[17]. In fact, availability of different polarimetric channels, combined with the use of scattering models, in principle allows independently retrieving the different parameters on which backscattering depends (soil moisture, surface roughness, vegetation density, and shape). In particular, some of the employed models also take into account the presence of double bounce and volumetric scattering mechanisms to consider the presence of vegetation [14], [16], [17]. However, here we focus on the methods tailored for bare or little vegetated soils, which only need modeling of the surface scattering component [8], [9], [12], [13], because this is the case of interest for Pol-SARAS simulations. Some of these methods [8], [9], [13] try to define appropriate combinations of the polarimetric channels chosen in such a way to be dependent on the minimum number of physical parameters of the observed scene: in the ideal case, they should be a function of the soil dielectric permittivity (and hence soil moisture) only; however, in practice, they also depend on the macroscopic roughness of the surface. In particular, in [8] and [9], lookup tables based on PTSM copol-crosspol and copol-corr graphs are used for the estimation of soil moisture in the presence of bare soil or low vegetation cover. The copol and crosspol ratios are defined in (20), and the correlation coefficient (corr) is defined as

$$\text{corr} = \frac{\left|\langle i_{\text{HH}} i_{\text{VV}}^{*}\rangle\right|}{\sqrt{\langle |i_{\text{HH}}|^2\rangle \langle |i_{\text{VV}}|^2\rangle}}. \tag{22}$$

For PTSM, the dependence on small-scale roughness parameters cancels out in the ratios in (20) and (22), so that these ratios only depend on the large-scale roughness $\sigma$ and on the relative dielectric permittivity $\varepsilon$. This is exploited in [9] to devise a method for the estimation of $\varepsilon$ from measured polarimetric data: the obtained estimates can be used for the estimation of the volumetric soil moisture, via appropriate mixing models [9]. In particular, in [9], a method based on the evaluation of the copol–crosspol graphs is used, whereas in [8], the use of copol–corr graphs is proposed, too. One enters the graphs with copol and crosspol ratios (or copol ratio and correlation coefficient) obtained from SAR data and reads the retrieved values of $\varepsilon$ and $\sigma$ on the graphs. (Of course, this can be done automatically by a computer program.)

Since, as already discussed, Pol-SARAS simulations have a wider range of validity than that of PTSM, they provide the possibility to generate graphs that are not subject to PTSM approximations. In the following, we discuss how the proposed simulator can be used to obtain the abovementioned graphs.

To evaluate the quantities in (20) and (22), we used the same simulated images of Section III-A. Once the three channels' images were obtained, we evaluated the quantities in (20) and (22) using a multilook of $8 \times 8$ pixels and then averaging over the whole scene, as discussed in Section III-A. Finally, we repeated the simulations for several values of $\varepsilon$ and $\sigma$, in order to obtain the copol–crosspol and copol–corr graphs. In Fig. 9, the graphs obtained for a look angle of 45° are reported. Similar results are obtained for look angles of 35° and 55°. The behavior of the graphs matches with PTSM theoretical expectations, at least in the considered range of $\varepsilon$ and $\sigma$ values [8], [9]. However, the presented graphs are expected to provide a range of validity wider than the PTSM-based ones, especially for small look angles. A unique characteristic of the Pol-SARAS simulator is the possibility to account for anisotropic features of terrain roughness. Indeed, in the simulator, it is possible to set two different values for the standard deviation of the facets' slopes in range and azimuth directions, i.e., $\sigma_x \neq \sigma_y$, see Section II-A. This possibility is particularly interesting in case of agricultural applications, where harvesting and vegetation growth can easily impose anisotropy on soil shape. The results for this case are shown in Fig. 10. The simulation parameters are those of Table I, with a look angle of 45° and $\varepsilon = 4$. In Fig. 10(a), we compare the results obtained for the copol–crosspol graph setting $\sigma_x = \sigma_y = \sigma$ (i.e., the isotropic case), with those obtained setting $\sigma_x = 0$ and $\sigma_y = \sqrt{2}\sigma$, or $\sigma_y = 0$ and $\sigma_x = \sqrt{2}\sigma$ (i.e., two anisotropic cases). The square root of two factor is used to make the graphs comparable, considering that the overall roughness in the case $\sigma_x = \sigma_y = \sigma$ can be expressed as $(\sigma_x^2 + \sigma_y^2)^{1/2} = \sqrt{2}\sigma$. As theoretically expected, since in the absence of azimuth slopes, cross-polarization is not present, when $\sigma_x = 0$ (i.e., only range slope and no azimuth slope),

TABLE V

COMPARISON OF $I_2$ FROM ACTUAL AND SIMULATED DATA FOR THE THREE ROI OF FIG. 7

| | YELLOW ROI | | BLUE ROI | | GREEN ROI | |
|---|---|---|---|---|---|---|
| | Mean value | Standard deviation | Mean value | Standard deviation | Mean value | Standard deviation |
| Actual SAR data | 1.78 | 1.49 | 1.71 | 1.37 | −0.89 | 1.86 |
| Simulated $\sigma$=0.1 | 1.87 | 1.07 | 1.90 | 1.07 | −1.81 | 0.79 |
| Simulated $\sigma$=0.15 | 1.82 | 1.15 | 1.81 | 1.18 | −1.76 | 0.86 |
| Simulated $\sigma$=0.2 | 1.62 | 1.36 | 1.64 | 1.39 | −1.72 | 0.91 |

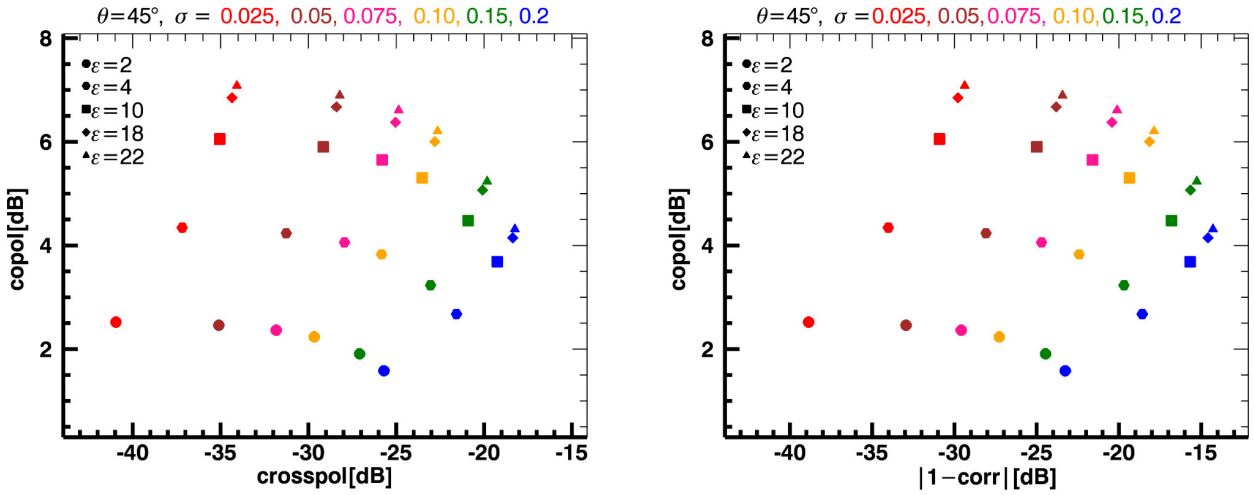


(a) (b)

Fig. 9. (a) Copol–crosspol and (b) copol–corr graphs for $\theta = 45°$. For visualization purposes, the absolute value of the copol ratio in dB is reported on the vertical axis.

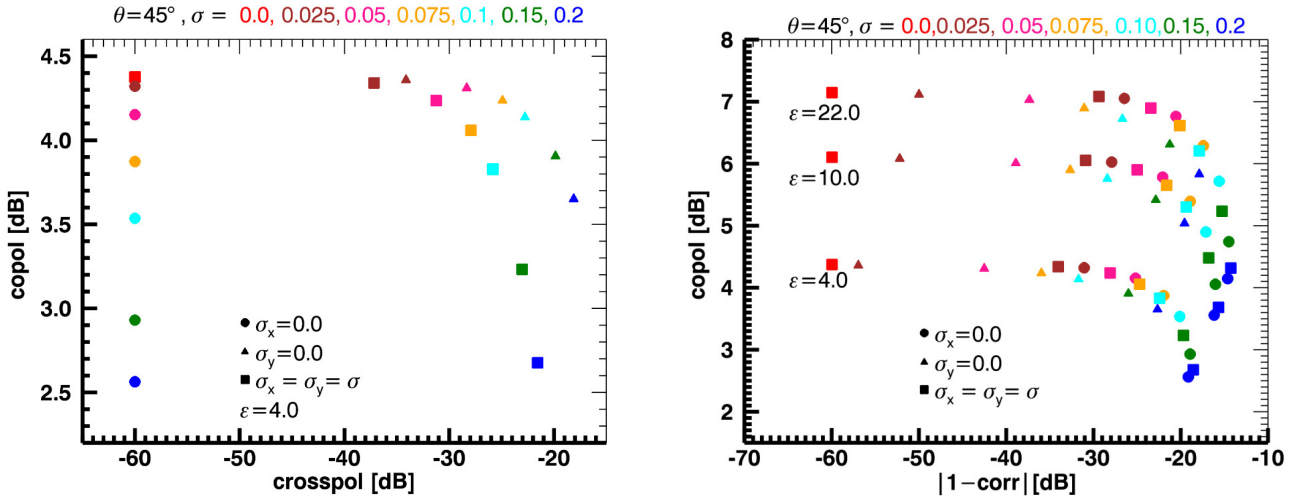


(a) (b)

Fig. 10. (a) Copol–crosspol and (b) copol–corr graphs in case of anisotropic soil roughness for $\theta = 45°$. For visualization purposes, the absolute value of the copol ratio in dB is reported on the vertical axis.

the crosspol ratio is practically 0 independent of $\sigma_y$ value; however, for visualization purposes in Fig. 10(a), we set it to the conventional value of −60 dB. Moreover, we notice that in this case, the values of copol ratio obtained for a certain $\sigma$ are slightly lower than those obtained in the case of $\sigma_x = \sigma_y = \sigma$. When $\sigma_y = 0$ (i.e., only azimuth slope and no range slope),

the results are somehow inverted. In particular, the range of variation of the copol ratio is smaller than that of the case $\sigma_x = \sigma_y = \sigma$; conversely, the range of the variation of the crosspol ratio is larger than that of the case $\sigma_x = \sigma_y = \sigma$. This is due to the high sensitivity of the crosspol ratio to azimuth slopes. From the viewpoint of soil-moisture estimation, i.e., of $\varepsilon$ estimation, it is evident that in the presence of significant anisotropy, the estimation is impaired, since $\varepsilon$ = constant curves are very far from those relevant to the isotropic case, especially when azimuth slopes are negligible with respect to range ones.

In Fig. 10(b), the results for the copol–corr graph are reported. When $\sigma$ is equal to 0, corr is equal to 1 and, hence, $(1 - \text{corr})$ is equal to 0: for visualization purposes in this case, we set $(1 - \text{corr})$ to the conventional value of $-60$ dB. Due to the strong dependence of both copol ratio and corr on range slopes, we note that the graph relevant to the case of $\sigma_x = 0$ is similar to the one obtained for $\sigma_x = \sigma_y = \sigma$, whereas the graph relevant to the case of $\sigma_y = 0$ significantly departs from the case $\sigma_x = \sigma_y = \sigma$. However, in this case, we note that $\varepsilon$ = constant curves in the presence of anisotropy are very close to those relevant to the isotropic case. This is demonstrated by plotting the points relevant to different values of $\varepsilon$, which highlights how the estimation of $\varepsilon$ is not significantly affected by anisotropic roughness. This is a very important result, suggesting that the use of copol–corr graphs should be preferred for bare-soil-moisture retrieval, whenever uncontrollable anisotropies may be present in the macroscopic roughness.

Let us now consider another application of SAR polarimetry, i.e., the rotation angle $\beta$ estimation for the compensation or the estimation of terrain azimuth slope variation [20]. In fact, in [20] and [27], it is shown that if surface scattering dominates and if $|\beta| \leq \pi/4$, then $I_2$ in (21) is equal to $4\beta$, so that it can be used to retrieve $\beta$ from polarimetric SAR data. Results presented in Section III-B on simulated polarimetric SAR data of Camp Roberts already visually show that as expected, and in agreement with real data, $I_2$ is actually related to azimuth mean terrain slope in the resolution cell via the rotation angle $\beta$ (see Fig. 7). For a quantitative assessment, as "ground truth" for the retrieval of $\beta$ from SAR data, we computed the $\beta$ angle for the considered scene from the available DEM (after averaging the latter to obtain the same 20 m $\times$ 20 m pixel spacing of the $I_2$ maps). Obtained mean $\beta$ values (computed by restricting $\beta$ values to the interval $|\beta| \leq \pi/4$) over the three regions of interest (ROI) selected in Section III-B are reported in Table VI, together with the mean $\beta$ values retrieved from real and simulated SAR data via (21). With regard to simulated data, we considered different, both isotropic and anisotropic, large-scale roughness conditions. In addition, in Table VI, we also report the mean $\beta$ values retrieved via (21) after a $2 \times 2$ boxcar smoothing on both real and simulated SAR data [so that averages in (21) are in this case obtained on $4 \times 72$ pixel windows]. Results from Table VI show that if no smoothing is applied to SAR data, then the following hold:

1) $\beta$ values retrieved from real SAR data are significantly underestimated (in absolute value), and this underestimation is higher on vegetated areas ("green" and "blue" regions).
2) $\beta$ values retrieved from simulated SAR data are also underestimated, but in better agreement to DEM-derived ones with respect to real data estimates; in addition, the underestimation increases as the large-scale roughness increases.
3) When anisotropic large-scale roughness is considered, the underestimation effect due to roughness is much more significant if roughness slopes are along the azimuth direction.

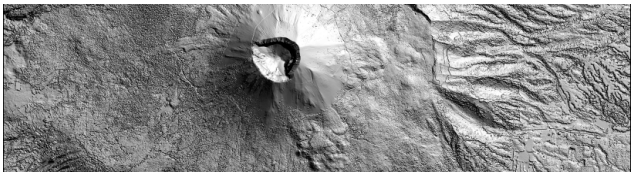

Fig. 11. Shaded representation of the smoothed LiDAR DEM of the Vesuvius volcano.

However, $\beta$ estimations after smoothing of polarimetric SAR data are in much better agreement with the DEM-derived ones, and effects of roughness, noise, and vegetation are significantly reduced. Also, retrievals from real and simulated data are in very good agreement, thus confirming that differences between real and simulated $I_2$ images in Fig. 7 are mainly due to unmodeled noise, see discussion in Section III-B.

In conclusion, simulated results show that if the elements of the coherency matrix are obtained by averaging over about 70–80 pixels (which is usually considered sufficient in most applications [1]), even for pure surface scattering, the retrieval of $\beta$ from SAR polarimetric data may be affected by underestimation due to surface roughness, especially if the latter is prevalently along the azimuth direction. However, this effect is almost completely eliminated if a further $2 \times 2$ averaging is performed, so that the overall averaging is over about 300 pixels.

Finally, to illustrate the application of the presented simulator to the assessment of classification methods based on polarimetric SAR data and to show the simulator efficiency in terms of processing time, we present a last example regarding a scene with a nonflat DEM, simulated giving as input to Pol-SARAS a one-meter-resolution LiDAR DEM of the volcano Vesuvius, close to Naples, Italy [23]. Since the high-resolution LiDAR DEM is too sensitive to the presence of vegetation and anthropogenic features, a preliminary smoothing step was applied, leading to a final resolution of 5 m. The DEM obtained after the smoothing is shown in Fig. 11. The simulations were performed using the parameters reported in Table I, with a look angle of 45°, a relative dielectric constant equal to 4. As an example, the HH channel simulated image is reported in Fig. 12: a multilook with a factor of 2 in range and 16 in azimuth is applied, to obtain an approximately square pixel.

Obtained results are here analyzed in terms of $H$ and $\alpha$ images obtained from the Pol-SARAS simulations. In Fig. 13, $H$ and $\alpha$ images obtained for $\sigma = 0.1$ are shown. The values of $H$ are low and tend to be higher in areas of low intensity. The values of $\alpha$ are low in average and tend to increase for

TABLE VI
MEAN VALUES OF $\beta$ [rad] RETRIEVED FROM DEM AND FROM ACTUAL AND SIMULATED DATA FOR THE THREE ROI OF FIG. 7

| | YELLOW ROI | | BLUE ROI | | GREEN ROI | |
|---|---|---|---|---|---|---|
| | No smoothing | 2 x 2 smoothing | No smoothing | 2 x 2 smoothing | No smoothing | 2 x 2 smoothing |
| DEM | 0.54 | 0.54 | 0.57 | 0.57 | –0.54 | –0.54 |
| Actual SAR data | 0.44 | 0.56 | 0.43 | 0.53 | –0.22 | –0.47 |
| Simulated $\sigma$=0.025 | 0.48 | 0.52 | 0.50 | 0.53 | –0.46 | –0.48 |
| Simulated $\sigma$=0.1 | 0.47 | 0.51 | 0.47 | 0.52 | –0.45 | –0.47 |
| Simulated $\sigma$=0.2 | 0.41 | 0.49 | 0.41 | 0.50 | –0.43 | –0.47 |
| Simulated $\sigma_x$=0.2, $\sigma_y$=0 | 0.38 | 0.49 | 0.35 | 0.46 | –0.41 | –0.48 |
| Simulated $\sigma_x$=0, $\sigma_y$=0.2 | 0.45 | 0.49 | 0.46 | 0.51 | –0.43 | –0.44 |

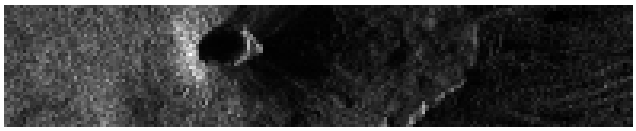

Fig. 12. Simulated image relevant to the HH channel.

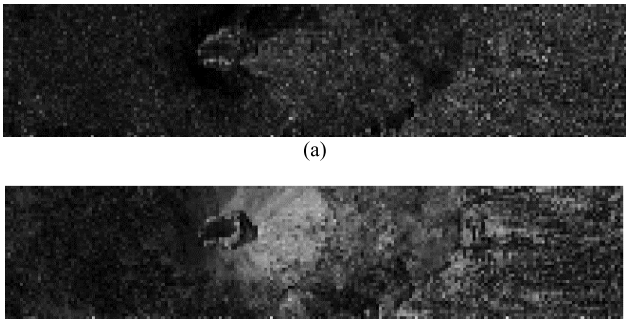

(a) (b)

Fig. 13. Images of (a) entropy and (b) $\alpha$ angle relevant to the Vesuvius simulation.

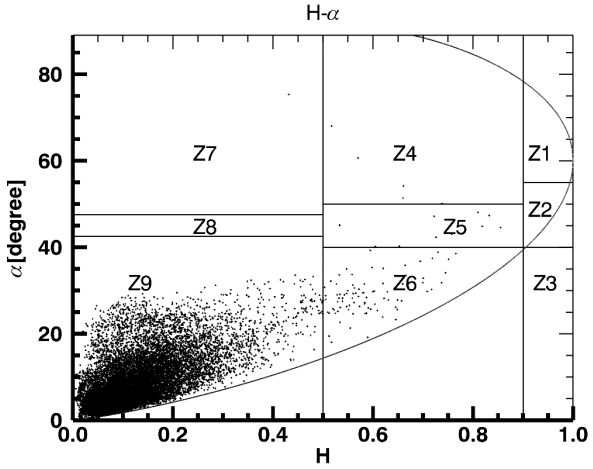


Fig. 14. Scatterplot of the images in Fig. 13 represented in the $H$–$\alpha$ plane partitioned according to the classification scheme proposed in [19].

increasing values of the local incidence angle, as expected. These observations are confirmed by the $H$–$\alpha$ scatterplot shown in Fig. 14, where the zones identified according to the classification scheme proposed in [19] are reported. The graph confirms that most of the points are located in zone 9, i.e., present low values of both entropy and $\alpha$. Zone 9 is indicative of the presence of surface scattering mechanisms [19].

A few last words on computation complexity and processing time are now due. First of all, it must be noted that computation complexity has not been significantly increased with respect to the non-polarimetric SARAS simulator, so that it is still approximately proportional to $N^* \log N$, where $N$ is the number of pixels for the considered scene. In fact, overall computational complexity for the three polarimetric channels is slightly less than three times the one for a single channel. (Consider that many operations for reflectivity generation are in common for the three channels, which compensates for the fact that generation of random deviations of facets' slopes has been added.) In particular, for the Vesuvius scene, with a 5261 × 1506 pixel raw signal size, on a general purpose PC with an Intel Core i7-6700HQ CPU @ 2.60 GHz and a 16-GB RAM, processing time is 47 s for SARAS and 2 min and 18 s for Pol-SARAS.

## IV. CONCLUSION

In this paper, a fully polarimetirc SAR simulator, which we named Pol-SARAS, has been presented. It is based on the use of sound direct electromagnetic models, and it is able to provide as output the simulated raw data of all the

three polarization channels in such a way as to obtain the correct covariance or coherence matrices on the final focused images. At the moment, the proposed simulator takes into account the surface scattering contribution only; however, thanks to the simulator modularity, volumetric and double-bounce contributions can be included to account for vegetation, too, if efficient and accurate models become available. Actually, several quite accurate vegetation models are already available (see [28], [29]), but their efficient implementation in the simulation scheme is not straightforward, and it is left to future work.

In addition, we also note that man-made complex targets (for instance, buildings in urban areas) may be considered by the proposed simulator by including them in the DEM (with also an appropriate complex permittivity, see Section II), but only provided that $z(x, y)$ remains single valued (i.e., two or more facets with the same $x$, $y$ coordinates and different heights cannot be considered). In addition, multiple bounces between different facets are not considered. For the non-polarimetric SARAS simulator, both limitations can be overcome as described in [30], but that solution cannot be easily extended to the Pol-SARAS case, and this has not been made for the moment being. Finally, the proposed polarimetric SAR simulation scheme can be applied to time-varying marine scenes by extending the approach described in [37], but this is not straightforward, and has not been implemented for the moment being.

The proposed simulator has been shown to provide results in agreement with what predicted by available theoretical models, at least in the validity ranges of the latter. In addition, polarimetric data obtained from simulated raw signals have been shown to agree with those obtained from a real SAR sensor. Finally, the potentialities of the simulator in support of some practical applications of SAR polarimetry have been investigated. In particular, with regard to soil-moisture retrieval, the possibility to simulate scenes presenting anisotropic macroscopic roughness has been exploited to demonstrate that the use of copol–corr lookup tables has to be preferred to copol–crosspol ones for the estimation of $\varepsilon$, in the presence of surfaces that may present an anisotropic roughness. Furthermore, with regard to the rotation angle estimation from polarimetric SAR data, presented results show that to avoid underestimation, sufficiently large windows must be used in computing the coherency matrix elements. Finally, the usefulness of the simulator for the analysis of polarimetric classification schemes has been also discussed: in particular, an example of the application of $H$–$\alpha$ analysis has been presented.

## REFERENCES


[1] J.-S. Lee and E. Pottier, *Polarimetric Radar Imaging: From Basics to Applications*. Boca Raton, FL, USA: CRC Press, 2009.

[2] G. Franceschetti, M. Migliaccio, D. Riccio, and G. Schirinzi, "SARAS: A synthetic aperture radar (SAR) raw signal simulator," *IEEE Trans. Geosci. Remote Sens.*, vol. 30, no. 1, pp. 110–123, Jan. 1992.

[3] S. Cimmino, G. Franceschetti, A. Iodice, D. Riccio, and G. Ruello, "Efficient spotlight SAR raw signal simulation of extended scenes," *IEEE Trans. Geosci. Remote Sens.*, vol. 41, no. 10, pp. 2329–2337, Oct. 2003.

[4] G. Franceschetti, R. Guida, A. Iodice, D. Riccio, and G. Ruello, "Efficient simulation of hybrid stripmap/spotlight SAR raw signals from extended scenes," *IEEE Trans. Geosci. Remote Sens.*, vol. 42, no. 11, pp. 2385–2396, Nov. 2004.

[5] G. Franceschetti, A. Iodice, S. Perna, and D. Riccio, "SAR sensor trajectory deviations: Fourier domain formulation and extended scene simulation of raw signal," *IEEE Trans. Geosci. Remote Sens.*, vol. 44, no. 9, pp. 2323–2334, Sep. 2006.

[6] G. Margarit, J. J. Mallorqui, J. M. Rius, and J. Sanz-Marcos, "On the usage of GRECOSAR, an orbital polarimetric SAR simulator of complex targets, to vessel classification studies," *IEEE Trans. Geosci. Remote Sens.*, vol. 44, no. 12, pp. 3517–3526, Dec. 2006.

[7] F. Xu and Y. Q. Jin, "Imaging simulation of polarimetric SAR for a comprehensive terrain scene using the mapping and projection algorithm," *IEEE Trans. Geosci. Remote Sens.*, vol. 44, no. 11, pp. 3219–3234, Nov. 2006.

[8] A. Iodice, A. Natale, and D. Riccio, "Polarimetric two-scale model for soil moisture retrieval via dual-Pol HH-VV SAR data," *IEEE J. Sel. Topics Appl. Earth Observ. Remote Sens.*, vol. 6, no. 3, pp. 1163–1171, Jun. 2013.

[9] A. Iodice, A. Natale, and D. Riccio, "Retrieval of soil surface parameters via a polarimetric two-scale model," *IEEE Trans. Geosci. Remote Sens.*, vol. 49, no. 7, pp. 2531–2547, Jul. 2011.

[10] F. T. Ulaby, R. K. Moore, and A. K. Fung, *Microwave Remote Sensing: Active and Passive*. Reading, MA, USA: Addison-Wesley, 1982.

[11] G. Franceschetti, A. Iodice, M. Migliaccio, and D. Riccio, "Scattering from natural rough surfaces modeled by fractional Brownian motion two-dimensional processes," *IEEE Trans. Antennas Propag.*, vol. 47, no. 9, pp. 1405–1415, Sep. 1999.

[12] J. Shi, J. Wang, A. Y. Hsu, P. E. O'Neill, and E. T. Engman, "Estimation of bare surface soil moisture and surface roughness parameter using L-band SAR image data," *IEEE Trans. Geosci. Remote Sens.*, vol. 35, no. 5, pp. 1254–1266, Sep. 1997.

[13] I. Hajnsek, E. Pottier, and S. R. Cloude, "Inversion of surface parameters from polarimetric SAR," *IEEE Trans. Geosci. Remote Sens.*, vol. 41, no. 4, pp. 727–744, Apr. 2003.

[14] I. Hajnsek, T. Jagdhuber, H. Schon, and K. P. Papathanassiou, "Potential of estimating soil moisture under vegetation cover by means of PolSAR," *IEEE Trans. Geosci. Remote Sens.*, vol. 47, no. 2, pp. 442–454, Feb. 2009.

[15] A. Iodice, A. Natale, and D. Riccio, "Retrieval of soil surface parameters via a polarimetric two-scale model in hilly or mountainous areas," *Proc. SPIE*, vol. 8179, pp. 817906-1–817906-9, Oct. 2011.

[16] T. Jagdhuber, I. Hajnsek, and K. P. Papathanassiou, "An iterative generalized hybrid decomposition for soil moisture retrieval under vegetation cover using fully polarimetric SAR," *IEEE J. Sel. Topics Appl. Earth Observ. Remote Sens.*, vol. 8, no. 8, pp. 3911–3922, Aug. 2015.

[17] G. Di Martino, A. Iodice, A. Natale, and D. Riccio, "Polarimetric two-scale two-component model for the retrieval of soil moisture under moderate vegetation via L-band SAR data," *IEEE Trans. Geosci. Remote Sens.*, vol. 54, no. 4, pp. 2470–2491, Apr. 2016.

[18] S. R. Cloude and E. Pottier, "A review of target decomposition theorems in radar polarimetry," *IEEE Trans. Geosci. Remote Sens.*, vol. 34, no. 2, pp. 498–518, Mar. 1996.

[19] S. R. Cloude and E. Pottier, "An entropy based classification scheme for land applications of polarimetric SAR," *IEEE Trans. Geosci. Remote Sens.*, vol. 35, no. 1, pp. 68–78, Jan. 1997.

[20] J.-S. Lee, D. L. Schuler, and T. L. Ainsworth, "Polarimetric SAR data compensation for terrain azimuth slope variation," *IEEE Trans. Geosci. Remote Sens.*, vol. 38, no. 5, pp. 2153–2163, Sep. 2000.

[21] X. Shen *et al.*, "Orientation angle calibration for bare soil moisture estimation using fully polarimetric SAR data," *IEEE Trans. Geosci. Remote Sens.*, vol. 49, no. 12, pp. 4987–4996, Dec. 2011.

[22] Y. Oh, K. Sarabandi, and F. T. Ulaby, "An empirical model and an inversion technique for radar scattering from bare soil surfaces," *IEEE Trans. Geosci. Remote Sens.*, vol. 30, no. 2, pp. 370–381, Mar. 1992.

[23] (Dec. 2009). *DSM, DTM Telerilevati Mediante Tecnologia Lidar*. [Online]. Available: http://sit.cittametropolitana.na.it/lidar.html

[24] G. Franceschetti, M. Migliaccio, and D. Riccio, "SAR raw signal simulation of actual ground sites described in terms of sparse input data," *IEEE Trans. Geosci. Remote Sens.*, vol. 32, no. 6, pp. 1160–1169, Nov. 1994.

[25] Y. L. Tong, *The Multivariate Normal Distribution*. New York, NY, USA: Springer-Verlag, 1990.

[26] *AIRSAR, Airborne Synthetic Aperture Radar*. Accessed: Jun. 2017. [Online]. Available: https://airsar.jpl.nasa.gov/

[27] J.-S. Lee, D. L. Schuler, T. L. Ainsworth, E. Krogager, D. Kasilingam, and W. M. Boerner, "On the estimation of radar polarization orientation shifts induced by terrain slopes," *IEEE Trans. Geosci. Remote Sens.*, vol. 40, no. 1, pp. 30–41, Jan. 2002.
[28] C. Yang, J. Shi, Q. Liu, and Y. Du, "Scattering from inhomogeneous dielectric cylinders with finite length," *IEEE Trans. Geosci. Remote Sens.*, vol. 54, no. 8, pp. 4555–4569, Aug. 2016.
[29] M. Kvicera, F. P. Fontán, J. Israel, and P. Pechac, "A new model for scattering from tree canopies based on physical optics and multiple scattering theory," *IEEE Trans. Antennas Propag.*, vol. 65, no. 4, pp. 1925–1933, Apr. 2017.
[30] G. Franceschetti, A. Iodice, D. Riccio, and G. Ruello, "SAR raw signal simulation for urban structures," *IEEE Trans. Geosci. Remote Sens.*, vol. 41, no. 9, pp. 1986–1995, Sep. 2003.
[31] O. Dogan and M. Kartal, "Efficient strip-mode SAR raw-data simulation of fixed and moving targets," *IEEE Geosci. Remote Sens. Lett.*, vol. 8, no. 5, pp. 884–888, Sep. 2011.
[32] H. Chen, Y. Zhang, H. Wang, and C. Ding, "SAR imaging simulation for urban structures based on analytical models," *IEEE Geosci. Remote Sens. Lett.*, vol. 9, no. 6, pp. 1127–1131, Nov. 2012.
[33] T. Yoshida and C.-K. Rheem, "SAR image simulation in the time domain for moving ocean surfaces," *Sensors*, vol. 13, no. 4, pp. 4450–4467, 2013.
[34] F. Zhang, C. Hu, W. Li, W. Hu, and H.-C. Li, "Accelerating time-domain SAR raw data simulation for large areas using multi-GPUs," *IEEE J. Sel. Topics Appl. Earth Observ. Remote Sens.*, vol. 7, no. 9, pp. 3956–3966, Sep. 2014.
[35] K.-S. Chen, L. Tsang, K.-L. Chen, T. H. Liao, and J.-S. Lee, "Polarimetric simulations of SAR at L-band over bare soil using scattering matrices of random rough surfaces from numerical three-dimensional solutions of Maxwell equations," *IEEE Trans. Geosci. Remote Sens.*, vol. 52, no. 11, pp. 7048–7058, Nov. 2014.
[36] B. Liu and Y. He, "SAR raw data simulation for ocean scenes using inverse Omega-K algorithm," *IEEE Trans. Geosci. Remote Sens.*, vol. 54, no. 10, pp. 6151–6169, Oct. 2016.
[37] G. Franceschetti, M. Migliaccio, and D. Riccio, "On ocean SAR raw signal simulation," *IEEE Trans. Geosci. Remote Sens.*, vol. 36, no. 1, pp. 84–100, Jan. 1998.

**Gerardo Di Martino** (S'06–M'09–SM'17) was born in Naples, Italy, in 1979. He received the Laurea degree (*cum laude*) in telecommunication engineering and the Ph.D. degree in electronic and telecommunication engineering from University of Naples Federico II, Naples, in 2005 and 2009, respectively.

From 2009 to 2016, he was with the University of Naples Federico II, where he was involved in applied electromagnetics and remote sensing topics. From 2014 to 2016, he was with the Italian National Consortium for Telecommunications and the Regional Center Information Communication Technology. He is currently an Assistant Professor of electromagnetics with the Department of Electrical Engineering and Information Technology, University of Naples Federico II. His research interests include microwave remote sensing and electromagnetics, with focus on electromagnetic scattering from natural surfaces and urban areas, synthetic aperture radar (SAR) signal processing and simulation, information retrieval from SAR data, and remote sensing techniques for developing countries.

**Antonio Iodice** (S'97–M'00–SM'04) was born in Naples, Italy, in 1968. He received the Laurea degree (*cum laude*) in electronic engineering and the Ph.D. degree in electronic engineering and computer science from the University of Naples "Federico II," Naples, Italy, in 1993 and 1999, respectively.

In 1995, he was with the Research Institute for Electromagnetism and Electronic Components, Italian National Council of Research, Naples. From 1999 to 2000, he was with Telespazio S.p.A., Rome, Italy. From 2000 to 2004, he was a Research Scientist with the Department of Electronic and Telecommunication Engineering, University of Naples "Federico II," where he has been a Professor of electromagnetics with the Department of Electrical Engineering and Information Technology, since 2005. He has been involved in several projects funded by the European Union, Italian Space Agency, Italian Ministry of Education and Research, Campania Regional Government, and private companies, as a Principal Investigator or a Co-Investigator. He has authored or co-authored more than 300 papers, of which more than 80 have been published in refereed journals. His research interests include microwave remote sensing and electromagnetics, modeling of electromagnetic scattering from natural surfaces and urban areas, simulation and processing of synthetic aperture radar signals, and electromagnetic propagation in urban areas.

Prof. Iodice received the "2009 Sergei A. Schelkunoff Transactions Prize Paper Award" from the IEEE Antennas and Propagation Society for the best paper published in 2008 in the IEEE TRANSACTIONS ON ANTENNAS AND PROPAGATION. He was recognized by the IEEE Geoscience and Remote Sensing Society as the 2015 Best Reviewer of the IEEE TRANSACTIONS ON GEOSCIENCE AND REMOTE SENSING. He is the Chair of the IEEE South Italy Geoscience and Remote Sensing Chapter.

**Davod Poreh** (M'17) was born in Takab, Iran. He received the bachelor's and master's degrees from the Engineering Department, University of Tehran, Tehran, Iran. He is currently pursuing the Ph.D. degree with the University of Naples Federico II, Naples, Italy.

Since 2014, he has been with the Department of Electrical Engineering and Information Technology, University of Naples Federico II. He has been involved in radar satellite/airborne remote sensing, laser remote sensing, and passive satellite remote sensing in many European countries including Germany and Italy. His research interests include microwave and passive remote sensing, image processing [both optical and synthetic aperture radar (SAR)], radar, polarimetric radar, interferometric SAR (InSAR), InSAR time series (persistent scatterers interferometry and SBAS), sensor design, polarimetric-based radar simulations, and information retrieval for land, oceanic, and urban area.

**Daniele Riccio** (M'91–SM'99–F'14) was born in Naples, Italy. He received the Laurea degree (*cum laude*) in electronic engineering from the University of Naples Federico II, Naples, in 1989.

He was a Research Scientist with the Italian National Research Council, Institute for Research on Electromagnetics and Electronic Components, Naples, Italy, from 1989 to 1994, a Guest Scientist with the German Aerospace Centre (DLR), Munich, Germany, from 1994 to 1995, a Lecturer of the Ph.D. Program with the Universitat Politecnica de Catalunya, Barcelona, Spain, in 2006, and with the Czech Technical University, Prague, Czech, in 2012. He is currently a Full Professor of electromagnetic fields with the Department of Electrical Engineering and Information Technology, University of Naples Federico II. He is also a member of the Cassini Radar Science Team. He is the Coordinator of the Ph.D. School in Information Technology and Electrical Engineering, University of Naples Federico II, and the Representative of the same university within the Assembly of the National Inter-University Consortium for Telecommunications and the Scientific Board of the Italian Society of Electromagnetism. He has authored three books, including *Scattering, Natural Surfaces and Fractals* (2007), and more than 400 scientific papers. His research interests include microwave remote sensing, electromagnetic scattering, synthetic aperture radar with emphasis on sensor design, data simulation, and information retrieval, as well as application of fractal geometry to remote sensing.

Prof. Riccio was a recipient of the 2009 Sergei A. Schelkunoff Transactions Prize Paper Award for the best paper published in 2008 in the IEEE TRANSACTIONS ON ANTENNAS AND PROPAGATION. He serves as an Associate Editor for several journals on remote sensing.